JOURNAL OF COMPUTATIONAL PHYSICS **128,** 381–390 (1996)
ARTICLE NO. 0218

Time-Domain Electromagnetic Scattering Simulations on Multicomputers

J. S. SHANG

Flight Dynamics Directorate, U.S. Air Force Wright Laboratory, Wright–Patterson Air Force Base, Ohio 45433

Received July 31, 1995; revised June 3, 1996

A series of bistatic radar cross sections of a perfectly conducting sphere over a frequency range were processed on one shared and three distributed memory computers. A comparative study was conducted for both the total field and the scattered field formulations. The accuracy criteria for the grid point density per wavelength and the placement of the truncated far-field boundary were also established for the present characteristic-based finite volume scheme. The numerical accuracy of all simulations has been validated with theoretical results.

INTRODUCTION

To date, the finite-difference and finite-volume methods for solving three-dimensional Maxwell equations in the time domain (FDTD or FVTD) have very limited practical applications ranges (1–3). The limitation arises from the unique features of truncation error in computing time-dependent phenomena and the low numerical efficiency of existing procedures. In essence, the truncation error in time dependent simulations leads to dissipation and dispersion which induces attenuated wave amplitude and phase shift (4). In order to control the quasi-physical effects of numerical simulations to be within an acceptable tolerance, a certain grid density must be maintained. For most popular second-order accurate numerical methods using an unstaggered mesh system, the rule of thumb is 15 nodes per wavelength (1, 3). However, the simple grid density criterion becomes insufficient when the computational domain contains multiple media with a wide range of characteristic impedances. For an electromagnetic simulation associated with a large-scale configuration at high frequencies, the required number of mesh points to meet an accuracy specification is often beyond the reach of conventional computing systems. Therefore, in high frequency spectra, the FDTD or FVTD schemes can only be used for simulations associated with compact dimensions. This limitation can be alleviated in principle through the development of more accurate algorithms for solving the basic governing equations, using scalable high performance computing systems, and a combination of both.

The inaccuracies incurred by numerical simulations are attributable to the mathematical formulation of the problem, the numerical procedure, and the computational accuracy. For the scattering simulation, the Maxwell equations in the time domain can be formulated in total-field and scattered-field variables (5, 6). In a homogeneous and isotropic medium where the governing equations are linear, the superposition principle prevails. Since all electromagnetic excitations satisfy the Maxwell equations, the scattered-field formulation can also be viewed as the result of a dependent variable transformation from the total field, and the system of equations is unaltered. The change in the differential system rests only on the imposition of initial and boundary conditions. The scattered-field formulation is frequently adopted for computing diffraction and refraction (1, 7). The advantage of the scattered-field formulation is easily understood: it eliminates completely the quasi-physical error involved in the incident wave when it propagates from the far-field boundary to the scatterer. This accuracy advantage is significant when the equivalent field theorem is invoked to accomplish the near-to-far-field transformation (8, 9). In the present investigation, the specific comparison of numerical results generated by the two formulations will be highlighted.

The physically incorrect value and the poor implementation of initial and boundary conditions are another major source of error in the computations. The appropriate placement and type of boundary/initial conditions also have a determining effect on the numerical accuracy. The Maxwell equations in the time domain constitute a hyperbolic system. Solutions of the equations system may not be analytic and have distinctive domains of dependence which are defined by eigenvalues of the governing equations (10). The demarcation between zones of dependence is described by characteristics. Along these time-space trajectories, the wave content is invariant. Therefore, the existence of characteristics permits the splitting of wave components according to the signs of phase velocity in each spatial direction (11–13). The directional information of a wave motion can be used equally effectively as an absorbing boundary condition (14–16) to suppress the spuriously reflected waves at the truncated computational boundary (3,

0021-9991/96 $18.00

11–13). On the scattering surface, the split flux is also essential for imposing the electric and magnetic field conditions simultaneously on an unstaggered grid system.

In practice, the dissipative and dispersive error of time-dependent calculations can be assessed and alleviated by grid refinement. For the scattering simulation, the placement of the computational far field becomes a concern. The objective of simultaneously minimizing the size of the computational domain and the contamination of reflected waves from the numerical boundary creates conflicting requirements. This numerical peculiarity is algorithm and computational procedure dependent. A grid refinement as well as a study of the placement of the far-field boundary is carried out in the present analysis. However, the basic approach to lifting the accuracy limitation must be derived using high-order schemes or spectral methods (17–19). Both approaches can yield numerical solutions of similar accuracy but at a much lower grid point density than that of the commonly used second-order schemes.

The computational efficiency can be enhanced substantially by using scalable multicomputers (20, 21). The effective use of a distributed memory, message-passing homogeneous multicomputer still requires a tradeoff between a balanced work load and interprocessor communication. In previous efforts, the characteristic-based finite-volume procedure has been successfully mapped onto the Intel Touchstone Delta and the Intel Paragon XP/S systems (22–24). In order to increase the potential for greater portability of the parallel computer code to a wider range of multicomputers, the parallelized version of the FVTD code is mapped onto an IBM SP2 and a Cray T3D system. The adopted message-passing interface libraries are the PVM (parallel virtual machine) and MPI (message-passing interface) (25, 26). Since the present one-dimensional domain decomposition strategy (22–24) is not designed to minimize node-to-node communication for a FDTD or FVTD algorithm, the performance of the combination of message length and transmitting frequency for practical applications will be recorded for future reference.

In the present investigation, the scattering phenomena are simulated on four high-performance computing systems using a cell-centered, upwind finite-volume scheme for time-dependent, 3D Maxwell equations (3, 12). Specifically, the radar cross sections (RCS) of a perfectly electrical conducting (PEC) sphere are computed by both the total-field and scattered-field formulations. The incident waves are time harmonic, linearly polarized in negative z axis (8). The wave numbers (k) have a range from 4.6 to 20 for which analytic solutions are known (6). The effects of placement of the truncated numerical domain and the grid density refinement on the RCS results are analyzed and delineated. Efforts are also made to define and validate the range of the parallel scalable performance of the present code. From the present investigation, an assessment of the engineering accuracy need and the range of scalability will be made to guide future research for high performance computing in CEM.

NUMERICAL ALGORITHM

The time-dependent Maxwell equations for the electromagnetic field can be given as (8, 9)

$$\frac{\partial B}{\partial t} + \nabla \times E = 0 \tag{1}$$

$$\frac{\partial D}{\partial t} - \nabla \times H = -J \tag{2}$$

$$\nabla \cdot B = 0, \qquad B = \mu H \tag{3}$$

$$\nabla \cdot D = 0, \qquad D = \varepsilon E, \tag{4}$$

where ε and μ are the electric permittivity and the magnetic permeability which relate the electric displacement to the electric field intensity and the magnetic flux density to the magnetic field intensity, respectively.

The time-dependent Maxwell equations can be cast in flux vector form on a general curvilinear and body conformal frame of reference by a coordinate transformation from the Cartesian system. The governing equations become (3, 12)

$$\frac{\partial U}{\partial t} + \frac{\partial F_\xi}{\partial \xi} + \frac{\partial F_\eta}{\partial \eta} + \frac{\partial F_\zeta}{\partial \zeta} = -J, \tag{5}$$

where U is the transformed dependent variable now scaled by the local cell volume, V; and F_ξ, F_η, and F_ζ are the contravariant components of the flux vectors of the Cartesian coordinates which are the basic frame of reference of the present analysis.

$$U = \{B_x V, B_y V, B_z V, D_x V, D_y V, D_z V\}^{\mathrm{T}} \tag{6}$$

$$F_\xi = (\xi_x F_x + \xi_y F_y + \xi_z F_z)V$$

$$F_\eta = (\eta_x F_x + \eta_y F_y + \eta_z F_z)V$$

$$F_\zeta = (\zeta_x F_x + \zeta_y F_y + \zeta_z F_z)V \tag{7}$$

where the flux vector components of the Cartesian frame are

$$F_x = \{0, -D_z/\varepsilon, D_y/\varepsilon, 0, B_z/\mu, -B_y/\mu\}^{\mathrm{T}}$$

$$F_y = \{D_z/\varepsilon, 0, -D_x/\varepsilon, -B_z/\mu, 0, B_x/\mu\}^{\mathrm{T}} \tag{8}$$

$$F_z = \{-D_y/\varepsilon, D_x/\varepsilon, 0, B_y/\mu, -B_x/\mu, 0\}^{\mathrm{T}}$$

and ξ_x, η_x, ζ_x, ξ_y, η_y, ζ_y, ξ_z, η_z, and ζ_z are the nine metrics of the coordinate transformation.

The total field formulation can be cast in the scattered field form by replacing the total field with scattered field variables (5, 6),

$$U_s = (U_t - U_i). \tag{9}$$

Since the incident field, U_i, must satisfy the Maxwell equations identically, equations of the scattered field remain unaltered from the total field formulation. Thus, the scattered field formulation can be considered as a dependent variable transformation from the total-field equations. For this reason, the notations in the scattered-field and the total-field formulations are indistinct in the subsequent derivations. In the present approach, both formulations are solved by a characteristic-based finite volume scheme. The discretized equations then degenerate into the balancing of a flux vector aligned with the surface area vectors (3, 12).

The characteristic-based finite-volume approximation is achieved by splitting the flux vector according to the signs of eigenvalues of the coefficient matrix in each spatial direction (27). The flux vector at any cell interface is represented by a superposition of two components from F_ξ^+, F_ξ^-, F_η^+, F_η^-, F_ζ^+, and F_ζ^- depending on the direction of the wave motion (3, 12). At the cell surfaces, the split flux vectors are calculated by the reconstructed dependent variables on either side of the interface according to the κ scheme (28, 29),

$$\begin{aligned} F_{\xi,i+1/2} &= F_\xi^+(U^{\mathrm{L}}_{i+1/2}) + F_\xi^-(U^{\mathrm{R}}_{i+1/2}) \\ F_{\eta,j+1/2} &= F_\eta^+(U^{\mathrm{L}}_{j+1/2}) + F_\eta^-(U^{\mathrm{R}}_{j+1/2}) \\ F_{\zeta,k+1/2} &= F_\zeta^+(U^{\mathrm{L}}_{k+1/2}) + F_\zeta^-(U^{\mathrm{R}}_{k+1/2}), \end{aligned} \tag{10}$$

where U^{L} and U^{R} denote the reconstructed dependent variables at the left and right sides of the cell interface, respectively.

A single-step, two-stage Runge–Kutta scheme is adopted for the temporal integration process. The resultant numerical procedure is capable of generating numerical solutions from first-order to third-order accurate in space and second-order accurate in time (3, 12).

INITIAL AND BOUNDARY CONDITIONS

The initial and boundary conditions for the perfectly conducting sphere can be summarized as follows. The incident wave consists of a linearly polarized harmonic field propagating in the negative z-axis direction (8).

$$\begin{aligned} B_y &= -A\sqrt{\varepsilon\mu}\,\sin(\omega t + kz) \\ D_x &= A\,\varepsilon\,\sin(\omega t + kz), \end{aligned} \tag{11}$$

where A denotes the amplitude of the incident wave. For the present investigation, the wave amplitude is assigned a value of unity.

Initially, the incident field is specified over the incoming half of the entire computational domain, and the downwind shadow domain remains unperturbed. This initial condition is preferred over the prescription of a completely quiescent computational domain for reducing the transient period of incident excitation.

The far-field boundary condition of the truncated numerical domain remains one of the most difficult problems encountered in computational electromagnetics (CEM) (1–3, 11). All numerical scattered field simulations in the time domain must be conducted in a truncated computational domain. Unavoidably, spurious wave reflections will take place at the artificial boundary. The reflected waves are known to induce inaccurate patterns for interacting waves and erroneous accumulations of radiation energy (3, 7, 11). In principle, if one of the coordinates is aligned with the direction of wave motion, the split flux of the characteristic-based scheme is identical to the compatible condition at the truncated far-field boundary. For the present formulation, an effective approximation is easily implemented by setting a null value for the incoming flux component in the radial direction. In the present simulation, the scattered field does not have spherical symmetry. Therefore, the vanishing incoming flux condition at the truncated far-field boundary degenerates into an approximation (11–13):

$$F_\xi^-(\xi_o, \eta, \zeta) = 0. \tag{12}$$

For simulations of a scattered field by a sphere, the solid surfaces are assumed to have perfect electrical conductivity. The appropriate boundary conditions at the surfaces of the sphere are (5, 8):

$$\begin{aligned} \mathbf{n} \times (E_1 - E_2) &= 0 \\ \mathbf{n} \times (H_1 - H_2) &= J_s \\ \mathbf{n} \cdot (B_1 - B_2) &= 0 \\ \mathbf{n} \cdot (D_1 - D_2) &= \rho_s. \end{aligned} \tag{13}$$

In short, on a perfect conductor surface the tangential component of the total electric field is required to vanish. This requirement implies that the normal component of the total magnetic field is zero on the conductor surface (8, 9). Thus, the electromagnetic field is discontinuous across the interface of the conductors. Following previous efforts (12, 13, 24), the unknown surface current and charge densities are treated as finite jumps of constant value. This formulation is compatible with the basic attribute of the hyperbolic partial differential system which allows the piecewise continuous data to propagate unaltered along a

characteristic (10). The following two extrapolated numerical boundary conditions for the finite jump properties at the surface are introduced to replace the equations that contain unknowns. It shall be emphasized that these extrapolations are approximated numerical boundary conditions.

$$\begin{aligned} \mathbf{n} \cdot \nabla(\mathbf{n} \times (H_1 - H_2)) = 0 \\ \mathbf{n} \cdot \nabla(\mathbf{n} \cdot (D_1 - D_2)) = 0 \end{aligned} \tag{14}$$

The system of boundary conditions is closed and applicable to the PEC sphere. The combination of the Dirichlet and the Neumann conditions forms two 3×3 matrices that are solved simultaneously for the electric and the magnetic field on the same mesh point. In so doing, the governing equations and the boundary conditions are fully satisfied on each and every mesh point of the calculated field. The consistent resolution is in contrast to solutions obtained from a staggered mesh system. Equally importantly, the imposed boundary conditions have been validated previously by comparing solutions generated from analytic boundary values (3, 5, 13).

RADAR CROSS-SECTION CALCULATION

The radar cross-section is a measure of the far-field distribution of electromagnetic energy from a scatterer. For a three-dimensional scattering body, the RCS is defined as (5)

$$\sigma(\theta, \phi) = \lim_{r \to \infty} 4\pi r^2 [H_s/H_i]^2 \tag{15}$$

or

$$\sigma(\theta, \phi) = \lim_{r \to \infty} 4\pi r^2 [E_s/E_i]^2. \tag{16}$$

The far-field asymptotes for the RCS computation, H_s and E_s, are expressible in terms of parameters associated with the near field by a near-field to far-field transformation (5, 9),

$$\begin{aligned} E(K, r) = (iK/4\pi) \int\int_S [\sqrt{\mu/\varepsilon}\,(\mathbf{n} \times H) \\ - (\mathbf{n} \times E) \times \mathbf{r} - (\mathbf{n} \cdot E)\mathbf{r}]\, e^{-iKr \cdot \mathbf{r}}\, dS \end{aligned} \tag{17}$$

$$\begin{aligned} H(K, r) = (iK/4\pi) \int\int_s [\sqrt{\varepsilon/\mu}\,(\mathbf{n} \times E) \\ + (\mathbf{n} \times H) \times \mathbf{r} + (\mathbf{n} \cdot H)\mathbf{r}]\, e^{-iKr \cdot \mathbf{r}}\, dS, \end{aligned} \tag{18}$$

where $\mathbf{n}$ and $\mathbf{r}$ denote the surface outward normal of the scatterer and the unit vector of the observation direction. In addition, the dependent variables of the integrand, E and H, are now the Fourier transform variables in the frequency domain (5, 9).

PARALLELIZATION PROCEDURE

All present results are processed on the Cray C916/16256, Cray T3D, IBM SP2, and Intel Paragon XP/S computing systems. The Cray C90 is the only shared memory system used and has a rated peak performance of 952 Mflops per processor. The vectorized version of the present computer code has achieved a data processing rate of 610 Mflops with an average vector length of 94.7. Since this code is thoroughly validated with a wide range of benchmarks (3, 12, 13) and demonstrates a reasonably high vectorized efficiency, it was utilized as the mainstay of the present effort. Among the three distributed memory systems employed, the Paragon XP/S has 388 i860XP nodes, while the other two systems have a 128-available-nodes configuration each. In terms of the raw data processing speed per node, the SP2 system leads the pack with a peak rate of 266 Mflops. The T3D and the Paragon XP/S have peak rates of 150 and 100 Mflops respectively. In practical applications, the data processing rate rarely approaches the rated peak performance.

For the distributed memory computing systems, the node-to-node and node-to-memory communication bandwidths also critically affect the parallel efficiency. For the Paragon, all nodes are connected to a mesh routing chip (MRC) through an interface module. The MRC has 10 unidirectional ports and a bandwidth of 200 Mb. On the SP2 system, communication is performed by a high performance switch (HPS) and there are multiple paths between any two nodes. The HPS has a peak bisection bandwidth of 2.5 Gb/S. For the T3D, the communication is carried by a three-dimensional torus and the peak bisection bandwidth is rated as high as 76.8 Gb/S to achieve the global addressable capability for all computing nodes. However, the parallel computing performance of any message passing multicomputers is closely tied to communication and latency. These features, peculiar to each system, are introduced by the communication protocol and operating system implementation which have a profound influence on the parallel efficiency.

In order to balance the work load and to enhance the portability of the parallelized code, the most elementary one-dimensional (1D) domain partition is adopted for the present investigation (22). In the present decomposition of the three-dimensional data structure (IL $\times$ JL $\times$ KL), each planar data array (JL $\times$ KL) is assigned to an individual computing node. As a consequence, the required number of computing nodes for a three-dimensional simulation is identical to the number of mesh points along one of the three coordinates. A clear advantage of the 1-D parallelization (22–24) is that the computer program conversion from

a shared to a distributed memory system becomes very straightforward. The computer program for a shared memory operation becomes the precise instruction for each individual node. Other data partition strategies, including the page structure, the pencil structure, and the block structure, may have some more degrees of control over data movement (22, 23). The mapping strategy is algorithm specific and an incisive grasp of system architecture is required in the coding efforts. The search for a better data structure partition remains as one of the pacing items toward high parallel efficiency for distributed memory computing systems.

The data movement of the earlier approach is controlled by a group of synchronous message passing calls (23, 24). Specifically, for each time step advancement, a minimum of 2 synchronous calls are issued from every node. A total of 2 $\times$ (IL-2) synchronous receptions and transmissions are performed. These calls are the absolute minimum necessary to transmit the six dependent variables and the flux vector associated with the node for the overlapping region of the difference equations. Since the first and the last nodes (1 and IL) are assigned to accommodate the less computing intensive boundary values along a coordinate direction, they are also used for outputting the formatted intermediate data. The message length is uniformly defined to be 48(JL $\times$ KL). Improvements have also been made to the parallelized code. Specifically, several asynchronous calls are inserted to enhance the overlapping of computation and communication. In addition, an option of using faster mathematical operations than the strict IEEE semantics (30) also was exercised for computations on the Paragon. Substantial improvement of numerical efficiency is noted.

NUMERICAL RESULTS

The presentation of numerical results is separated into two groups. The first group summarizes the performance of the present characteristic-based finite-volume code using 1D parallelization on the IBM SP2, the Cray T3D, and the Intel Paragon computing systems. The second group and the major portion of the present effort details four computations of a PEC sphere over a wave number range from 4.6 to 20.0. Since the sphere is assigned a diameter of unity, the parameters of the validating Mie series have the values of 2.3, 4.7, 5.3, and 10.0 (6, 9). The computational domain of all the cases studied is bounded by two concentric spheres, and is easily accommodated by the spherical coordinate system. The inner sphere describes the unit spherical scatterer, the outer sphere defines the truncated far-field boundary. The accuracy of RCS calculations is examined in light of the difference between total-field and scattered-field formulations, and the effects of grid-point density, and the placement of the far-field boundary. For the stated purpose, the third-order in space and second-order in time option of the computer code was used.

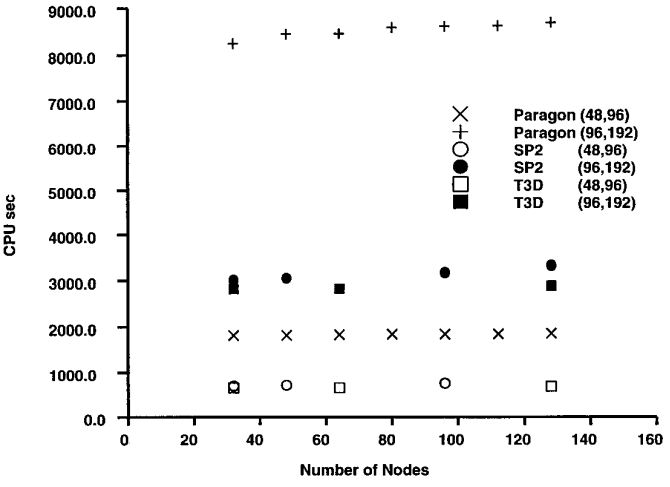

FIG. 1. Scalable performance on distributed-memory computing systems.

In Fig. 1, the timing results of two partitioned mesh systems (Node $\times$ 48 $\times$ 96) and (Node $\times$ 96 $\times$ 192) from three distributed memory computers are given. The message lengths of the two mesh systems span the range from 221,184 to 884,736 bytes. For the present data decomposition, the message length and the message passing frequency are linearly proportional to the size of the partitioned mesh system and the computing nodes in use, respectively. The timing result is defined as the execution time required by the present code to perform 600 time sweeps over the entire computational domain. For the smaller grid dimension, the scalability of the present version of the parallelized code is reasonable. Over the number of nodes tested, the present code has a scalable performance (based on 32 nodes performance) on the Cray T3D, Paragon XP/S, and IBM SP2 of 98.1, 97.9, and 91.8%, respectively. The code has the most efficient data processing rate (DPR) on T3D (1.115 sec), followed by SP2 (1.254 sec) and Paragon XP/S (3.026 sec). The timing results on the larger grid dimension indicate a progressively decreased parallel efficiency of 97.83, 94.88, and 90.57 on T3D, Paragon XP/S, and SP2 respectively. The DPRs from the three systems uniformly exceed a factor of 4 in comparison with the small mesh dimension calculations, the ratio of total mesh points between the two mesh systems. The DPR are 4.79 on T3D, 5.507 sec on SP2, and 14.367 sec on Paragon XP/S. This performance behavior is a clear indication that the contention of communication path becomes significant for the mesh system greater than (128 $\times$ 96 $\times$ 192). Among the three distributed systems, the Cray T3D has a global addressable capability in data communication through a three-dimensional torus. For this reason, the communica-

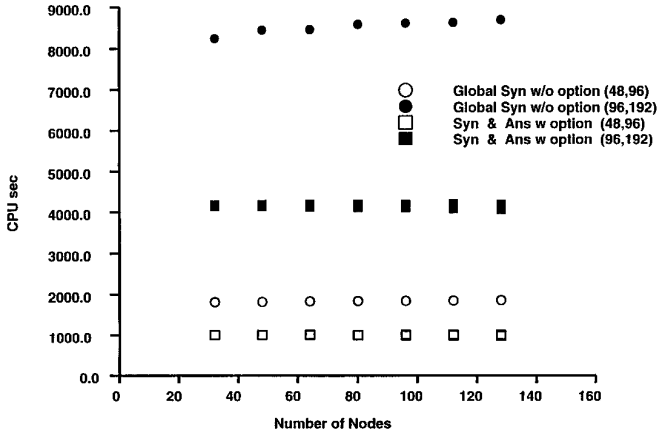

FIG. 2. Numerical efficiency enhancement on the Paragon XP/S computer.

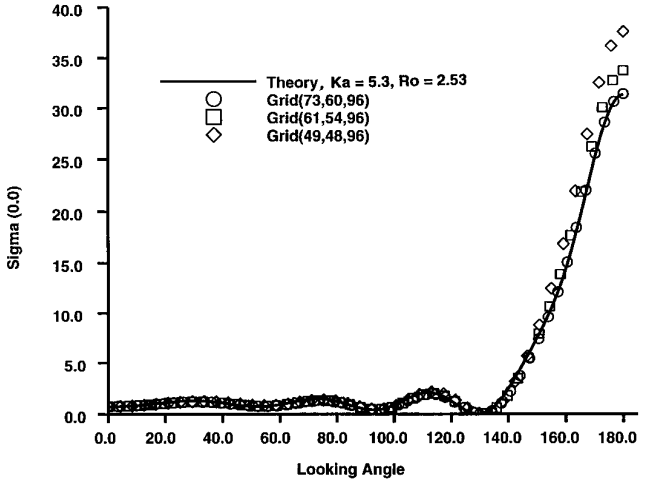

FIG. 3. Grid refinement study for RCS calculation, $\sigma(\theta, 0.0)$.

tion dominant code has the best scalable parallel performance on the Cray T3D system.

The parallel performances of the present code on the IBM SP2 and the Cray T3D are unavailable for a large mesh system using more than 128 nodes. The scalable performance on the Paragon XP/S degrades discernibly when more than 160 nodes are used concurrently (23, 24). The scalable performance of the present code on the XP/S is in general more than 2.7 times slower than the rate on either the IBM SP2 or the Cray T3D. A substantial amount of improvement is achieved by replacing global synchronous message passing calls with several asynchronous calls, using the nonstandard IEEE mathematical operation and a page locking option of the OSF/1 operating system to minimize the paging faults. The numerical efficiency improvement is presented in Fig. 2. On the smaller mesh dimension, the data processing time reduces from 1840.6 to 990.5 seconds on 96 nodes. The reduction on the large mesh (Node $\times$ 96 $\times$ 192) is from 8608.0 to 4091.8 seconds. These numerical efficiency improvements are by factors of 1.86 and 2.10 respectively. Additional efficiency improvement for the present code is still possible; however more effective means may have to be derived from a better data partition approach (22). In essence, a sustained effort must be maintained to realize the full potential of scalable parallel systems.

The effect of grid density per wavelength on the RCS computational accuracy by the scattered-field formulation is presented in Figs. 3 and 4. For a unit sphere illuminated by a linearly polarized harmonic field with a wave number of 10.6, the ka (a is the radius of the sphere) parameter of the Mie series then has a value of 5.3 (6). The far-field boundary is placed at a distance of 2.53 wavelengths away from the scatterer. Three grid systems (49 $\times$ 48 $\times$ 96), (61 $\times$ 54 $\times$ 96), and (73 $\times$ 60 $\times$ 96), were investigated, resulting in a grid point density per wavelength of about 10.0, 12.0, and 15.0. The varying grid spacings are accommodated in the radial (r) and the azimuthal (θ) coordinates, while the circumferential angular displacement ($\nabla\phi$) remains at a constant value of 4°. Figure 3 depicts the normalized bistatic RCS, $\sigma(\theta, 0.0)$, for the three different simulations in linear scales. It clearly demonstrates that the present calculation generated by a grid density of 15 points per wavelength attains perfect agreement with the analytic results (6, 9). On the linear scale, the numerical discrepancies of the coarser mesh computations appear to concentrate in the shadow region of the scatterer, but the deviations are nearly uniformly distributed over the entire viewing angles.

The normalized bistatic RCS in vertical polarization, $\sigma(\theta, 90.0)$ for ka = 5.3, is presented in Fig. 4. The numerical error pattern is identical to that of the $\sigma(\theta, 0.0)$. At the grid point density per wavelength of 10.0 and 12.0, the

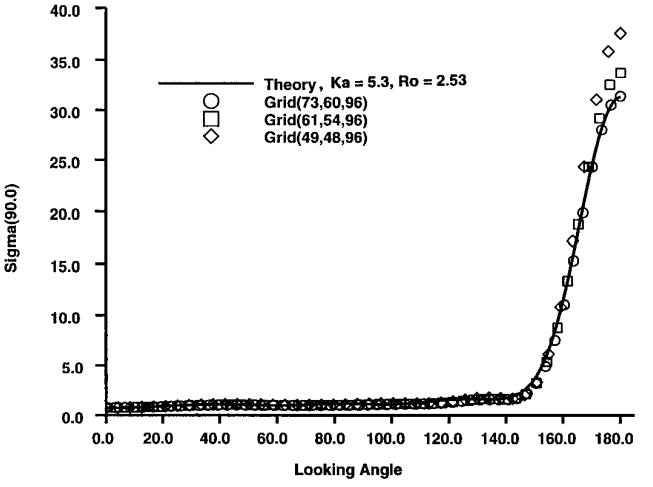

FIG. 4. Grid refinement study for RCS calculation, $\sigma(\theta, 90.0)$.

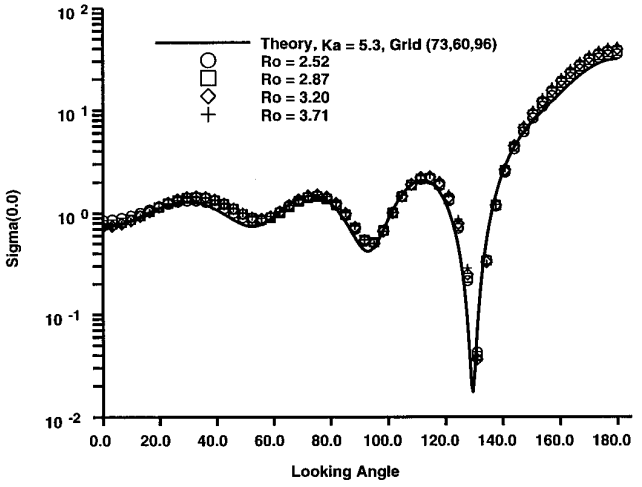

FIG. 5. Effect of farfield placement on RCS calculation, $\sigma(\theta, 0.0)$.

maximum numerical errors are 19.1 and 7.7 percent respectively. The accuracy improvement is rather drastic as the grid point density is enriched. For the result generated by the mesh of 15 points per wavelength, the maximum numerical result is reduced to less than one-quarter of 1%. Although the present numerical results are generated on a grid with an equal increment of all independent variables (∇r, $\nabla\theta$, $\nabla\phi$), the contiguous cell volumes still became highly stretched by the spherical coordinate system. The formal order of accuracy of any finite-volume scheme will degrade on an irregular and highly stretched mesh system (12). Thus, most spatially second-order accurate schemes may require an even higher grid point density per wavelength to yield a solution of precision comparable to the present approach.

The influence of far-field boundary placement on numerical accuracy is depicted in Figs. 5 and 6. The placement of the numerical boundary encounters two conflicting requirements in computation. In order to minimize the truncation error, the truncated boundary should be placed as close to the scatterer as possible. Meanwhile, the unperturbed incident boundary condition must also be located sufficiently far from the scatterer to avoid causing significant interference of the diffracted waves. Therefore, the placement of the truncate boundary is strongly affected by the numerical algorithm and the implementation of the farfield boundary conditions. At a wave number of 10.6, four different locations of the far field are analyzed. The far fields are placed at 3.71, 3.20, 2.87, and 2.52 wavelengths away from the scatterer which correspond to distances of 2.70, 2.40, 2.20, and 2.00 diameters away from the coordinate origin. Both the horizontal and vertical polarized bistatic RCSs, $\sigma(\theta, 0.0)$ in Fig. 5 and $\sigma(\theta, 90.0)$ in Fig. 6, exhibit a progressive and consistent improvement in numerical accuracy, until r reaches a value equal to 2.5 wavelengths. Further reduction in the size of the computational domain by placing the truncated boundary at a distance of less than 2.5 wavelengths from the scatterer leads to a greater than 1% departure from the theoretical back scattering value (6). For the ka = 5.3 simulations, the pure linearly polarized incident field can no longer be accurately imposed as the incoming condition at a distance closer than 2.5 wavelength from the scatterer. At any closer placement of the far-field boundary to the scatterer, the incoming far field will have to describe the interaction result of the incident and the diffraction. Indirectly, the present results also demonstrate that the characteristic-based method intrinsically is an efficient and effective means for far-field boundary condition implementation.

The pioneer efforts in RCS calculation usually employed the total-field formulation on staggered mesh systems (2, 31, 32). The particular combination of numerical algorithm and procedure has been proven to be very effective. The total-field formulation was also utilized in conjunction with the characteristic-based procedure in earlier RCS calculations (13, 24). An alternative approach via the scattered-field formulation for RCS calculations has just been demonstrated. The relative merit of these two formulations in numerical accuracy for RCS computations has not yet been quantified. The comparison of horizontally polarized RCS, $\sigma(\theta, 0.0)$, of the total-field and the scattered-field formulations at ka = 5.3 is presented in Fig. 7. Both numerical results are generated under identical computational conditions. The location of the truncated farfield boundary is prescribed by a value of 2.5 wavelengths from the PEC sphere. Numerical results of the total-field formulation revealed far greater error than the scattered-field formulation. The additional source of error is incurred when the incident wave must propagate from the far-field boundary to the scatterer. In the scattered-field formulation, the inci-

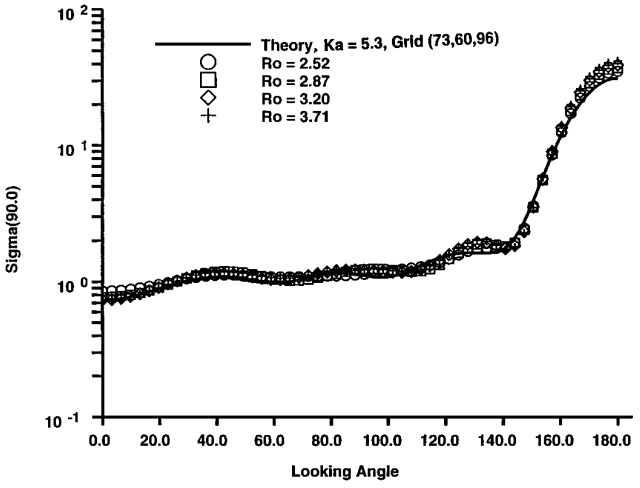

FIG. 6. Effect of farfield placement on RCS calculation, $\sigma(\theta, 90.0)$.

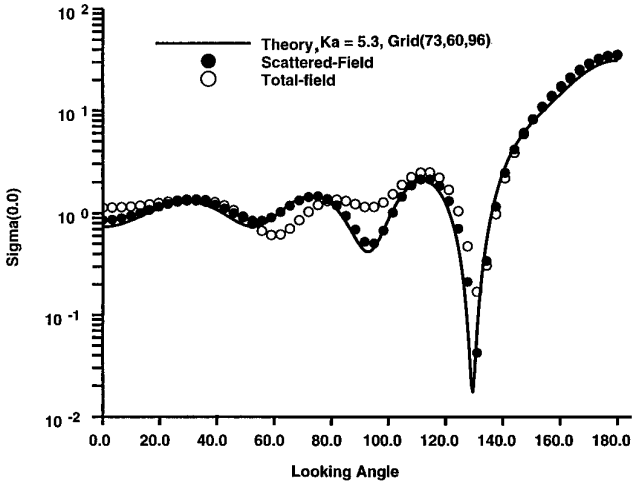

FIG. 7. Comparison of total-field and scattered-field formulation, $ka = 5.3$ $\sigma(\theta, 0.0)$.

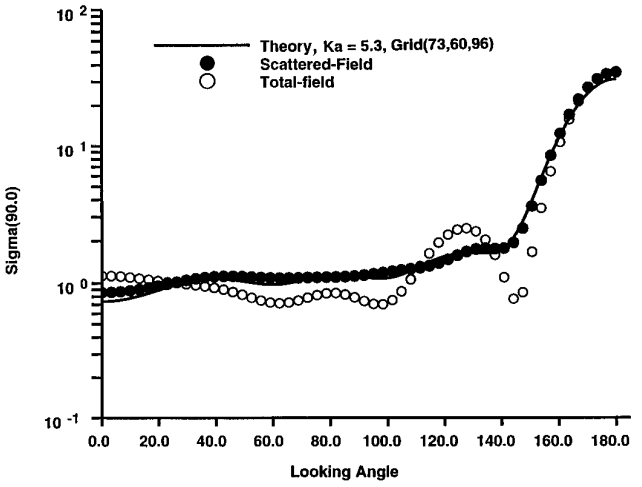

FIG. 8. Comparison of total-field and scattered-field formulation, $ka = 5.3$ $\sigma(\theta, 90.0)$.

dent field data are described precisely by the boundary condition on the scatterer surface. Since the far-field electromagnetic energy distribution is derived from the near field parameters (5, 6, 9), the advantage of describing the incident data without error on a scatterer is tremendous. The accumulated numerical errors in RCS computation through the integral transformation process manifest in the predicted magnitude over the entire range of viewing angles.

In Fig. 8, the vertically polarized RCS $\sigma(\theta, 90.0)$ of the ka = 5.3 case substantiates the previous observations. In fact, the numerical error of the total-field calculation is excessive in comparison with that of the scattered-field formulation. Results of the scattered-field formulation overpredict the theoretical value by 2.7%. The deviation of the total-field result from the theory however exceeds 25.6% and is unacceptable. In addition, computations by the total-field formulation exhibit a strong sensitivity to the placement of the far-field boundary. A small perturbation of the far-field boundary placement leads to a drastic change in RCS prediction: a feature resembling the ill-posedness condition which is highly undesirable for numerical simulation. Since there is very little difference in computer coding for the two formulations, computing times required for identical simulations are insignificant. On the Cray C90, 1,505.3 s at a DPR of 528.8 Mflops is needed to complete a sampling period. At present, the most efficient calculation on a distributed memory system has reduced the processing time to 1,204.2 seconds.

Similar behaviors of solutions generated by the total-field and the scattered-field at a lower frequency, ka = 2.3, are also observed. At the lower frequency, the theoretical far-field limit reduces to 1.462 diameters from the sphere. The numerical resolution requirement becomes even more stringent. Solutions generated by both formulations show excellent agreement on a $(73 \times 48 \times 96)$ grid and have a difference greater than a few percent on a $(49 \times 48 \times 96)$ grid. The former is supported by a fine grid density per wavelength of 24.96. Since we are interested in extending the application range of the present approach to high frequency, the detailed comparison is not presented here.

Another important issue of RCS calculations is the time elapsed for the transient period to subside after the initial incidence and the sampling duration. Figure 9 depicts the difference between the sampling durations of one and two periods (1.3659 seconds) after the transition period. The difference between two calculated RCSs, $\sigma(\theta, 0.0)$, is about 1.6% and is concentrated at the viewing angle of 59.5°. In the present analysis, the transient period of a scattering

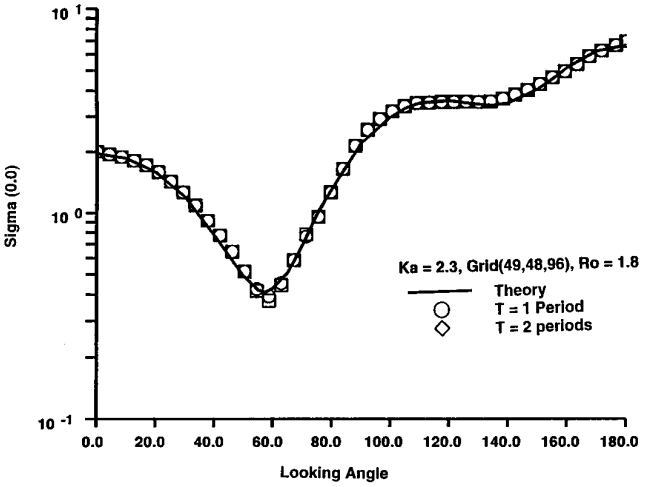

FIG. 9. RCS of a PEC sphere, $ka = 2.3$ $\sigma(\theta, 0.0)$.

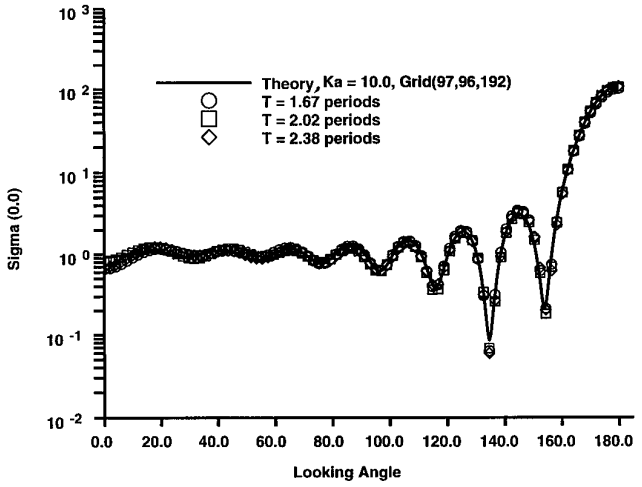

FIG. 10. RCS of a PEC sphere, $ka = 10.0$ $\sigma(\theta, 0.0)$.

phenomenon is defined as the time elapsed from the instant that a harmonic incident wave is introduced at the incoming farfield until a periodic diffraction pattern is established. By monitoring the magnetic surface current and the electric surface charge in the shadow region on the sphere, a harmonic diffraction is detected after an elapsed time equal to about 4.5 periods (24). The rather lengthy transient period is required if the entire simulated field is assumed to be quiescent initially. More efficient numerical procedures have been devised by imposing the impingement of incidence at the start. The transient period is observed to reduce by a factor of two. In any event, the present RCS results have demonstrated the achievement of a statistically stationary state.

The highest frequency computation of the present analysis using the scattered-field formulation is for a wave number of 20 and the ka parameter of 10. For this simulation, the farfield boundary is placed 3.0 wavelengths away from the sphere. A ($97 \times 96 \times 192$) mesh system is adopted to yield a grid point density per wavelength of 16.167. The initial condition is prescribed at the instant that the unperturbed incident just begins to illuminate the sphere. The bistatic RCSs are sampled at elapsed times of 1.667, 2.017, 2.377 periods (the duration of one period is 0.3142 s). Only the horizontally polarized bistatic RCSs distributions, $\sigma(\theta, 0.0)$, are given in Fig. 10. It is observed that the RCS calculations have reached an acceptable statistically stationary state after an elapsed time of about two periods. The maximum deviation among all three results is confined to within 4.7% and the difference between the last two samplings is less than 1.3%. The data processing time for a sampling period on the Cray C90 is 12,475.9 s at a data processing rate of 613.4 Mflops. The best performance of the present parallel code on a distributed memory processor still requires 9,984.9 s to process the identical case. It is obvious that substantial improvement of parallel numerical efficiency is urgently needed for CEM applications.

CONCLUDING REMARKS

A finite-volume, characteristic-based procedure for solving the time-dependent, three-dimensional Maxwell equations has been mapped onto three distributed memory computers, the Intel Paragon XP/S, the IBM SP2, and the Cray T3D. For the present one-dimensional data partitioning approach, the most efficient scalable parallel performance is achieved on the T3D system. Additional effort to realize fully scalable high performance computing is still urgently required.

In the PEC sphere radar cross-section calculations over a range of frequency and dimension parameters, $2.3 < \text{ka} < 10.0$, the scattered-field formulation is superior by far to the total-field formulation. Under identical simulation conditions, the scattered-field formulation not only generates more accurate RCS but also has a more robust numerical behavior than that of the total-field formulation.

On a unified mesh system, the present characteristic-based code needs a 15 grid point per wavelength density for the scattering simulations to achieve engineering accuracy. The present method also exhibits an attractive and effective feature for farfield boundary condition implementation. For most of the cases simulated, the far-field boundary is placed as close as 2.5 wavelengths away from the sphere.

APPENDIX: NOMENCLATURE

B	Magnetic flux density
D	Electric displacement
E	Electric field intensity
H	Magnetic field intensity
i, j, k	Indices of discretized volume
J	Electric current density
k	Wave number, $2\pi/\lambda$
$\mathbf{n}$	Surface outward normal
r, θ, ϕ	Spherical polar coordinates
R_o	Radius of outer sphere
S	Surface of a control volume
t	Time
U	Dependent variable
V	Elementary cell volume
ξ, η, ζ	General curvilinear coordinates
ε	Electric permittivity
μ	Magnetic permeability
λ	Wave length
σ	Normalized RCS
ω	Angular frequency
Superscripts	Flux component associated with
$+, -$	positive and negative eigenvalue
T	Transpose of a vector

ACKNOWLEDGMENTS

The assistance of Stephen Scherr and Paul Work of Wright-Patterson AFB and of Chris McArdle of Eglin AFB in porting the computer program onto the Intel Paragon XP/S and the Cray T3D systems is deeply appreciated. The author also gratefully acknowledges computing support from the Department of Defense HPC Shared Resource Centers at CEWES, Eglin, Maui, and WPAFB. This effort is supported by AFOSR and monitored by Dr. A. Nachman.

REFERENCES

1. V. Shankar, *Research to Application—Supercomputing Trends for the 90's and Opportunities for Interdisciplinary Computations,* Tech. Rep. AIAA 91-0002, Jan. 1991.
2. A. Taflove, *Comput. Systems in Engrg.* **3**(1–4), 153, (1992).
3. J. S. Shang, and D. Gaitonde, *Characteristic-Based, Time-Dependent Maxwell Equations Solvers on a General Curvilinear Frame,* Tech. Rep. AIAA 93-3178; also *AIAA J.* **33**(3), 491 (Mar. 1995).
4. D. A. Anderson, J. C. Tannehill, and R. H. Pletcher, *Computational Fluid Mechanics and Heat Transfer* (McGraw–Hill, New York, 1984).
5. J. W. Crispin, and K. M. Seigel, (Eds.), Methods of Radar Cross-Section Analysis, Academic Press, New York, 3–32, (1968).
6. J. J. Bowman, T. B. A. Senior, and P. L. E. Uslenghi, (Eds.), Electromagnetic and Acoustic Scattering by Simple Shapes, Hemisphere, New York, 353–415, (1987).
7. R. W. Noack, and D. A. Anderson, Time domain solutions of Maxwell's equations using a finite-volume formulation, in *30th AIAA Aerospace Science Meeting, Reno, NV, Jan. 6–9, 1992.*
8. R. F. Harrington, Time-Harmonic Electromagnetic Fields, McGraw-Hill Co., New York, (1961).
9. J. A. Stratton, Electromagnetic Theory, McGraw-Hill Co., New York, 1941.
10. R. Courant, and D. Hilbert, *Methods of Mathematics Physics,* Vol. II (Interscience, New York, 1965).
11. J. S. Shang, A Fractional-Step Method for the Time Domain Maxwell Equations, AIAA 93-0461, Jan. 1993; also *J. Comp. Phys.* **118**(1), 109–119, (April 1995).
12. J. S. Shang, IEEE Antennas and Propagation Mag. **37**(3), 15–25, (June 1995).
13. J. S. Shang, and D. Gaitonde, Scattered Electromagnetic Field of a Reentry Vehicle, AIAA 94-0231; also *AIAA J. Spacecraft and Rockets,* **32**(2), 294–301, (March–April 1995).
14. B. Enquist, and A. Majda, Math of Comput. **31,** 629–651, (July 1977).
15. R. Higdon, *Math of Comput.* **47**(176), 437–459, (1986).
16. G. B. Blaschak, and G. G. Kriegsmann, *J. Comp. Phys.* **77,** 107–139, (1988).
17. S. K. Lele, *J. Comp. Phys.,* **103,** 16–42, (1992).
18. S. T. Yu, L. S. Hultgren, and N. S. Liu, *AIAA J.* **32**(9), 1766–1773, (Sept. 1994).
19. C. Canuto, M. Y. Hussaini, P. Quarteroni, and T. A. Zang, *Spectral Methods in Fluid Dynamics* (Springer-Verlag, New York/Berlin, 31, (1988).
20. H. P. Flatt, and K. Kennedy, *Parallel Computing,* **12,** 1–20, (1989).
21. G. Bell, Ultracomputers, *Comm. ACM,* **35**(8), 27–47, (August 1992).
22. J. S. Shang, K. C. Hill, and D. A. Calahan, Performance of a Characteristic-Based, 3-D, Time Domain Maxwell Equations Solver on the Intel Touchstone Delta, AIAA 93-3179, July 1993; also *Appl. Comp. Electr. Soc.,* **10**(1), 52–62, (March 1995).
23. J. S. Shang, D. A. Calahan, and B. Vikstrom, Performance of a Finite Volume CEM Code on Multicomputers, AIAA 94-026; also *Comp. Sys. Engg.* **6**(3), 241–250, (1995).
24. J. S. Shang, and C. C. Shang, Concurrent Computation of Electromagnetic Phenomena on the Paragon, AIAA 95-0592.
25. J. Dongarra, A. Geist, R. Manchek, and V. Sunderam, *Comput. in Phys.,* **7**(2), 166–175, (April 1993).
26. V. Bala, S. Kipnis, L. Rudolph, and M. Snir, Designing Efficient, Scalable, and Portable Collective Communication Libraries, IBM Tech Rep., T. J. Watson Research Center, Oct. 1992, preprint.
27. P. L. Roe, *Ann Rev Fluid Mech,* **18,** 337–365, (1986).
28. W. K. Anderson, J. L. Thomas, and B. Van Leer, A Comparison of Finite Volume Flux Splittings for the Euler Equations, AIAA 85-0122; also *AIAA J.,* **24**(9), 1453–1460, (Sept. 1986).
29. J. L. Thomas, and R. W. Walter, *AIAA J.* **25**(4), 527–534, (April 1987).
30. Intel Corp., *Paragon User's Guide,* Publication 312489-002, (Oct. 1993).
31. K. S. Yee, *IEEE Trans. Antennas and Propagation,* **AP-14,** 302–307, (May 1966).
32. K. Umashankar, and A. Taflove, *IEEE Trans. Electromag. Compatibility,* **EMC-24**(4), 397–405, (Nov. 1982).